Responses of polar energy budget to regional SST changes in extra-polar regions

Qingmin Wang[1], Yincheng Liu[1], Lujun Zhang[1], Chen Zhou[1,*]

[1]School of Atmospheric Science, Nanjing University, Nanjing, 210000, China

5   *Correspondence to*: Chen Zhou (czhou17@nju.edu.cn)

Abstract. Surface temperature at polar regions is not only affected by local forcings and feedbacks, but also depends on teleconnections between polar regions and low latitude regions. In this study, the responses of energy budget in polar regions to remote sea surface temperature (SST) changes are analysed using a set of idealized regional SST perturbation experiments. The results show that responses of polar energy budget to remote sea surface warmings are regulated by changes in atmospheric

10   energy transport, and radiative feedbacks also contribute to the polar energy budget at both the top-of-atmosphere (TOA) and surface. Specifically, an increase of poleward atmospheric energy transport to polar regions results in an increase of surface and air temperature, and the corresponding Planck feedback leads to a radiative warming at surface and radiative cooling at TOA. In response to sea surface warmings in most midlatitude regions, the poleward atmospheric energy transport to polar regions in the corresponding hemisphere increases. Sea surface warming over most tropical regions enhances the polar energy

15   transport to both Arctic and Antarctic regions, except that an increase in the Indian Ocean's temperature results in a decrease in poleward atmospheric energy transport to the Arctic due to different responses of stationary waves. Sensitivity of Arctic energy budget to tropical SST changes is generally stronger than that of Antarctic energy budget, and poleward atmospheric heat transport is dominated by dry static energy, with a lesser contribution from latent heat transport. Polar energy budget is not sensitive to SST changes in most subtropical regions. These results help explain how the polar climate is affected by the

20   magnitude and spatial pattern of remote SST change.

1 Introduction

As global surface temperature increases, the Arctic region has experienced a surface temperature rise more than twice the global average (Lenssen et al., 2019), a phenomenon known as "Arctic Amplification" (AA). On the other hand, the Antarctic warming is weaker compared to the Arctic warming due to higher average elevation of the Antarctic continent, lower albedo,

25   feedback efficiency differences, and the Southern Ocean's heat absorption capacity (Marshall 2003; Salzmann et al., 2017; Smith et al., 2019; Hahn et al., 2021). The polar energy budget is highly sensitive to various local feedback mechanisms. One important mechanism is the ice-albedo feedback. Global warming reduces snow cover and sea ice cover in the polar regions, leading to more solar radiation being absorbed, which in turn accelerates climate warming and further decreases albedo (Dickinson et al., 1987; Hall, 2004; Boeke and Taylor, 2018; Duan et al., 2019; Dai et al., 2019). Temperature feedback is

30   another significant contributor to AA (Pithan and Mauritsen, 2014; Laîné et al., 2016; Sejas et al., 2016). It involves the processes of radiative cooling and is characterized by the Planck and lapse-rate feedbacks. The Planck feedback, driven by the nonlinear relationship between blackbody radiation and temperature, provides negative feedback to TOA fluxes at all latitudes, especially in low latitudes (Pierrehumbert, 2010). The lapse-rate feedback is a significant driver of AA: in the Arctic regions, stable stratification and temperature inversions trap surface warming and reduce radiative cooling, thereby enhancing warming.

35   In contrast, the tropics experience significant upper-atmosphere warming due to convection, which does not similarly trap heat (Pithan and Mauritsen, 2014). During climate warming, the transformation of ice clouds into water clouds increases cloud albedo, leading to negative feedback (Mitchell et al., 1989; Li and Le Treut, 1992). Simultaneously, the decrease in lower tropospheric stability increases Arctic cloud cover and optical thickness (Barton et al., 2012; Solomon et al., 2014; Taylor et al., 2015; Yu et al., 2019), contributing to Arctic autumn and winter warming (Boeke and Taylor, 2018). These local feedbacks

40   are considered primary contributors to Arctic amplification (Pithan and Mauritsen, 2014; Goosse et al., 2018; Hahn et al., 2021; Dai et al., 2019).

Polar climate is also affected by remote influences, whose interaction drives Arctic warming (Li et al., 2021). While some studies suggest that remote forcing plays a relatively minor role in Arctic amplification (Stuecker et al., 2018), other research highlights the significant impact of poleward heat and moisture transport from lower latitudes in enhancing Arctic warming,

45   and AA exists even in the absence of local sea-ice feedbacks (Alexeev et al., 2005; Graversen and Burtu, 2016). Specifically, poleward atmospheric heat transport (AHT) and moisture transport are critical components that contribute substantially to the observed warming in the Arctic.

Under global warming, the AHT from low latitudes is more effective in reaching the polar regions compared to the equatorward transfer from high latitudes (Alexeev et al., 2005; Chung and Räisänen, 2011; Park et al., 2018; Shaw and Tan, 2018; Semmler

50   et al., 2020), and multiple global climate model experiments have been conducted to measure the remote influence on Arctic warming (Alexeev et al., 2005; Chung and Räisänen, 2011; Yoshimori et al., 2017; Park et al., 2018; Shaw and Tan, 2018; Stuecker et al., 2018; Semmler et al., 2020). The transport of water vapor from mid-latitudes also plays an important role by enhancing the greenhouse effect prior to condensation and increasing cloudiness after condensation, which together warm the Arctic during winter (Graversen and Burtu, 2016). Graversen and Burtu (2016) showed that latent heat transport can lead to

55   significantly more Arctic warming than dry static energy (DSE) transport, even when delivering an equivalent amount of energy. Therefore, remote processes play an important role in driving Arctic warming, and the remote forcings are further amplified by local feedback processes.

In low-latitude regions, SST variations markedly affect the polar energy budget (Alexeev et al., 2005). It is widely accepted that planetary waves play a critical role in establishing teleconnections between tropical oceans and polar regions. These waves

60   are pivotal in the transport of heat and moisture to the Arctic, consequently driving the increase in polar temperatures (Graversen and Burtu, 2016; Baggett and Lee, 2017). For instance, intensified convective activity within the Pacific Warm Pool not only strengthens the propagation of Rossby waves toward the poles but also increases the frequency of these fluctuations. This enhancement in Rossby wave activity boosts the transport of water vapor to the Arctic, augmenting the

downward longwave radiation in the Arctic regions (Rodgers et al., 2003; Lee et al., 2011; Lee, 2012; Lee, 2014). While synoptic-scale transient eddies contribute significantly to mean-state poleward heat transport and its changes under increased CO2 (Donohoe et al., 2020), their overall impact is relatively minor compared to that of amplified planetary waves in responses to tropical warming (Baggett and Lee, 2017). Atmospheric circulation models reveal that warming of tropical SST from glacial to interglacial periods significantly elevates summer temperatures in regions where the Canadian ice sheet forms. Conversely, cold tropical SST perturbations exert a lesser impact on water vapor transport and temperature in the Canadian region (Rodgers et al., 2003). The tropical SST anomalies during El Nino and La Nia events have large impact on Arctic surface air temperature (Lee et al., 2011; 2012; 2014), but the impacts of major El Niño events on Arctic temperatures are distinct due to differences in eastern tropical Pacific SST (Jeong et al., 2022), indicating that the amplitude and spatial pattern of SST change is important for Arctic climate predictions.

In previous research, scholars primarily focused on the impact of SST over a large area of tropical oceans on the polar energy budget. However, studies have indicated significant variations in the effects of SST anomalies in different oceanic regions on the global climate system (Barsugli and Sardeshmukh, 2002; Fletcher et al., 2011). In this study, we employ a set of idealized SST patch experiments to perform a systematic analysis on the response of the polar energy budget to SST changes in various areas.

2 Data and Method

2.1 Individual patch experiments

The patch experiments were conducted using the Community Earth System Model version 1.2.1 integrated with the Community Atmospheric Model 5.3 (CESM1.2.1-CAM5.3, Neale et al. (2012)), operating at a spatial resolution of 1.9° latitude by 2.5° longitude. The experimental setup included a control experiment and two sets of patch experiments—one with warm patches and another with cold patches. The control experiment spanned 41 years, maintaining the sea surface temperature (SST), sea ice, and climatic forcings at the constant present-day levels observed in the (year 2000). The global ocean was segmented into 80 overlapping rectangular areas, comprehensively covering the global ice-free ocean surface, as depicted in Figure 1 of Zhou et al. (2020). In the warm patch experiments, a positive SST anomaly was introduced at the ocean surface within a designated patch, while the SST in other regions is same as the control setup. Conversely, the cold patch experiments involved introducing a negative SST anomaly at the ocean surface within the respective patches. The SST anomalies in each patch were designed according to the equation proposed by Barsugli and Sardeshmukh (2002), which effectively mitigates nonlinearity due to unrealistic SST gradients, ensuring a more realistic simulation of oceanic temperature variations,

$$\Delta SST_P(lat, lon) \quad = A \cos^2\left(\frac{\pi}{2}\frac{lat - lat_p}{lat_w}\right)\left(\frac{\pi}{2}\frac{lon - lon_p}{lon_w}\right), \tag{1}$$

where $|lat - lat_p| < lat_w$, $|lon - lon_p| < lon_w$. The terms lat_p and lon_p are the latitude and longitude of the center point for a specific patch, respectively; lat_w and lon_w are the meridional and zonal half-width of the patch, respectively, with their values set to $lat_w = 10°$ and $lon_w = 40°$ in these experiments; and A is the amplitude of the SST anomaly, which is set to be +4 K and -4 K in this study.

In this study, we analyzed the responses of polar TOA radiative fluxes (R_{TOA}), polar surface fluxes (R_{sfc}), and heat fluxes resulting from atmospheric heat transport to the polar regions (R_{AHT}). The equations for calculating these parameters are listed as follows:

$$R_{TOA} = FSNT - FLNT , \tag{2}$$

$$R_{sfc} = FSNS - FLNS - SH - LH , \tag{3}$$

$$R_{AHT} = R_{sfc} - R_{TOA} , \tag{4}$$

where $FSNT$ represents the net downward shortwave radiation at the TOA, $FLNT$ denotes the net upward longwave radiation at the TOA, $FSNS$ is the net downward shortwave radiation at the surface, $FLNS$ represents the net upward longwave radiation at the surface, and SH and LH account for the sensible and latent heat fluxes, respectively. Additionally, both SH and LH are defined as positive upward.

2.2 EOF-SST experiments

To quantify the polar energy budget response to realistic SST anomaly patterns, we applied EOF analysis to historical SST data from 1980 to 2019, and identified the first eight EOF modes. The first eight EOF modes explain approximately 55% of the total variance in global SST anomalies, thereby representing the predominant variability patterns. We then conducted eight separate EOF-SST experiments, and the SST of each experiment was perturbed by a specific EOF mode relative to the control run. These experiments allow us to isolate and understand the impact of realistic SST anomaly patterns on the polar energy budget.

2.3 Radiative Kernel Decomposition Methodology

This study employs the radiative kernel approach (Soden et al., 2008, Huang et al., 2017) to decompose both surface and TOA radiation into the radiative effects of various meteorological variables, measured in watts per square meter (Wm^{-2}). The core calculation involves multiplying the radiative kernels with the monthly anomalies of the corresponding climate fields as follows:

$$\Delta R_X = K_X \cdot \Delta X, \tag{5}$$

where X denotes an arbitrary non-cloud climate variable, ΔR_X represents the radiative effect at the surface or TOA associated with that variable, K_X is the corresponding radiative kernel, and ΔX is the monthly anomaly of the climate variable, calculated as the deviation from the monthly climatological average. Positive values of ΔR indicate an increase in net incoming radiation,

4

which corresponds to a warming effect on the Earth. The radiative kernels used in this analysis are derived from the ERA-Interim climatological fields and have been validated to perform well with climate model surface outputs (Huang et al., 2017; Liu et al., 2024).

Cloud radiative effects are calculated following the methodology of Soden et al. (2008):

$$\Delta R_{cld} = \Delta \text{CRF} - \sum_X (K_X - K_X^0) \Delta X \tag{6}$$

In this equation, ΔR_{cld} denotes the cloud-induced radiative anomalies, and CRF (Cloud Radiative Forcing) is defined as the difference in surface net radiation fluxes between all-sky and clear-sky conditions. The superscript [0] means the clear-sky kernels.

Building upon this framework, the study further decomposes the TOA and surface radiative anomalies into specific feedback components to achieve a more detailed analysis of the factors influencing the Earth's radiation balance. ΔR_{TOA} is partitioned into cloud-induced radiative anomalies ($\Delta R_{TOA,cld}$), albedo-induced radiative anomalies ($\Delta R_{TOA,alb}$), Planck feedback-induced radiative anomalies ($\Delta R_{TOA,plk}$), and lapse-rate feedback-induced radiative anomalies ($\Delta R_{TOA,LR}$). Similarly, ΔR_{sfc} is broken down into cloud-induced surface radiative anomalies ($\Delta R_{sfc,cld}$), albedo-related surface radiative anomalies ($\Delta R_{sfc,alb}$), Planck feedback-induced surface radiative anomalies ($\Delta R_{sfc,plk}$), lapse-rate feedback-induced surface radiative anomalies ($\Delta R_{sfc,LR}$), LH anomalies (ΔLH) and SH anomalies (ΔSH).

3 Result

3.1 Responses of Polar Energy Budget to Local SST Changes

The differences of annual polar energy budget in conjugate SST patch warming experiments and SST cooling experiments are shown in Figure 1. The location of each point denotes the center of corresponding patch, and the colors of these points denote the differences of polar energy budget between corresponding conjugate warming and cooling patch experiments. Additionally, t-tests were conducted to assess their statistical significance. The difference between TOA radiation (Figures 1a, d) and surface radiation (Figures 1b, e) reflects atmospheric heat transport (Figures 1c, f).

Figures 1(a-c) show the responses of the Arctic energy budgets to SST warmings in global oceanic regions. In response to western and central tropical Pacific SST warming, there is a significant increase in poleward energy transport towards the Arctic regions (Figure 1c), as indicated by the positive poleward heat transport to the Arctic region (positive ΔR_{AHT}). This enhanced energy transport warms the Arctic atmosphere, leading to an increase in surface radiation (positive ΔR_{sfc}, Figure 1b) due to higher surface and air temperatures. Simultaneously, the warmer atmosphere emits more longwave radiation to space, resulting in a decrease in TOA radiation (negative ΔR_{TOA}, Figure 1a). Conversely, warming in the tropical Indian Ocean reduces the poleward energy transport to the Arctic region (negative ΔR_{AHT}), leading to cooler Arctic atmospheric temperatures, and there is a decrease in surface radiation (negative ΔR_{sfc}, Figure 1b) and increase in TOA radiation (positive

ΔR_{TOA}, Figure 1a). Sea surface warming in the midlatitudes of the northern hemisphere increases Arctic surface radiation, but has insignificant impact on TOA radiation.

155   For the Antarctic energy budget, warming in the tropical Pacific and Indian Oceans generally leads to increased poleward energy transport (positive ΔR_{AHT}, Figure 1f), which warms the Antarctic atmosphere and results in increased Antarctic surface radiation (positive ΔR_{sfc}, Figure 1e) and decreased Antarctic TOA radiation (negative ΔR_{TOA}, Figure 1d). However, the response of ΔR_{TOA} to warmings in the tropical Atlantic is positive (Figure 1d). Warming in the Southern Ocean also leads to an increase of Antarctic surface radiation and decrease in Antarctic TOA radiation. Antarctic energy budget is generally not

160   sensitive to warmings in subtropical regions. Both ΔR_{TOA} and ΔR_{sfc} decrease in response to warmings in patches centred at 60°S, because patches centred at 60°S cover part of the Antarctic region (60°S to 90°S in this study), and the surface emit more energy to space as the sea surface warms, leading to a cooling radiative effect.

    The response of Arctic ΔR_{AHT} to tropical warmings is generally greater than Antarctic ΔR_{AHT}, indicating that more heat is transported to the Arctic region than that to the Antarctic region when the tropics warms. This difference may partly contribute

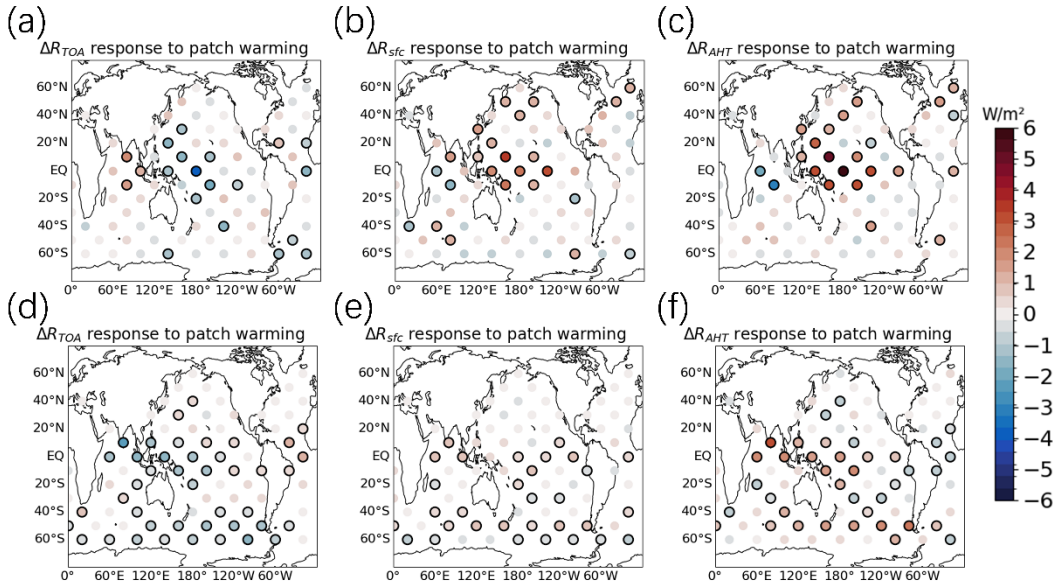165   to the faster Arctic warming than Antarctic warming under global warming.

Figure 1: Responses of polar energy budget to regional SST changes. (a) Differences of Arctic (60°N-90°N) annual mean net TOA radiative fluxes (ΔR_{TOA}) between conjugate warming and cooling patch experiments. (b) Differences of Arctic annual mean net surface radiative fluxes (ΔR_{sfc}), (c) Differences of heat fluxes due to atmospheric heat transport to the Arctic regions (ΔR_{AHT}). (d-
170   **e) Responses of ΔR_{TOA}, ΔR_{sfc}, and ΔR_{AHT} in the Antarctic regions. The location of each point denotes the center of corresponding patch, and the colors denotes the differences between conjugate warming and cooling patch experiments. Black circles denote that the differences are statistically significant at 95% confidence level.**

The responses of polar energy budget depend on the season. The spatial distribution of the Arctic polar energy budget response

175   to regional SST in boreal winter (DJF) (Figure 2a-c) is similar to the annual average values (Figure 1a-c), but the magnitude of DJF responses is greater than annual responses. For the Antarctic region, the response of DJF polar energy budget to tropical ocean warming aligns with the annual average values.
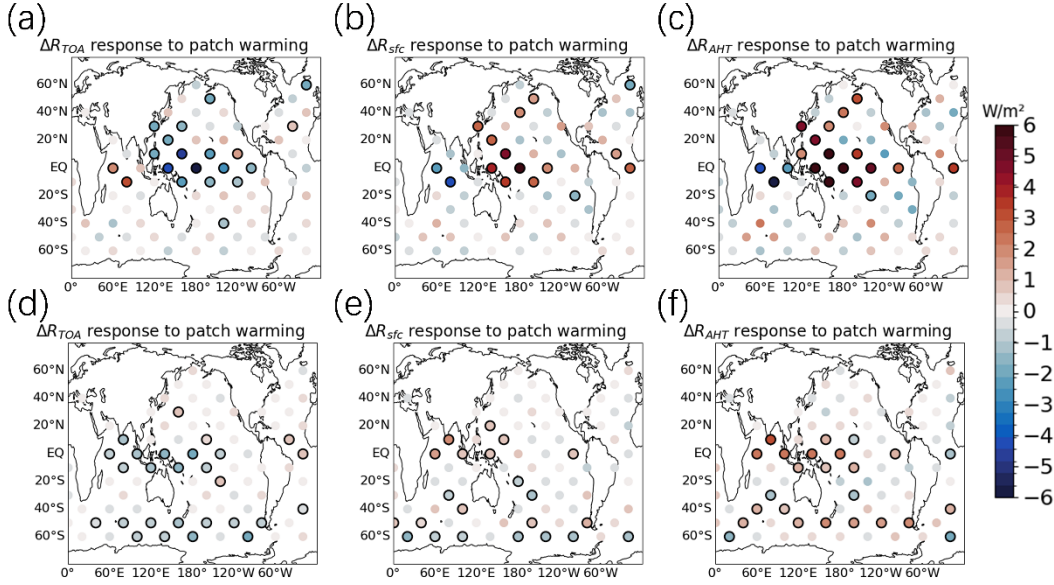

Figure 2: Same as Figure 1, but for the DJF season.

180

During boreal summer (JJA), the spatial distribution of Arctic polar energy budget responses (Figures 3a-c) differ from the annual average. Specifically, the responses of ΔR_{AHT} to warmings in both the Indian Ocean and western Pacific Ocean are positive. The responses of ΔR_{sfc} and ΔR_{TOA} in most patch experiments are statistically insignificant. Conversely, the Antarctic polar energy budget responses to tropical ocean warming in JJA are similar to annual mean values.
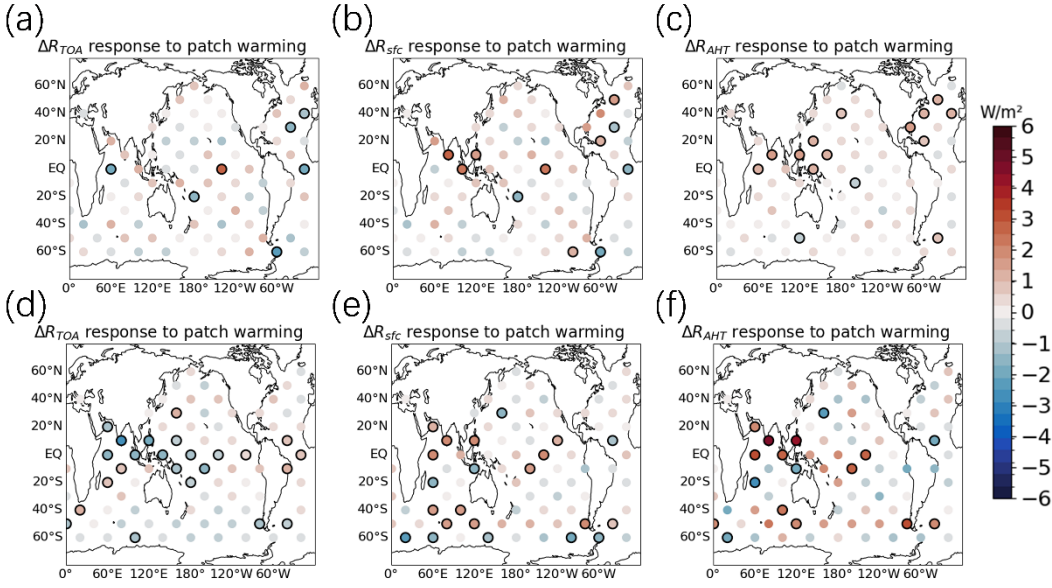
Figure 3: Same as Figure 1, but for the JJA season.

3.2 Reconstruction Using Green's Function

The response of polar energy budget to regional SST changes might be used to qualitatively explain how SST variations affect polar energy budget.

The sensitivity of the polar energy budget to SST perturbations within a specific grid box, identified by index i, can be estimated using the following equation (Zhou et al. 2017):

$$\left(\frac{\partial R}{\partial SST_i}\right)_p = \frac{\sum_P \Delta SST_P \frac{\partial R}{\partial SST_P} \frac{S_i}{S_P}}{\sum_P \Delta SST_P}, \tag{7}$$

where R denotes a specific energy flux, SST_i denotes the SST in the i-th grid box, S_i and S_P represent the ocean surface area of the specific grid point and the patch, respectively, and ΔSST_P is the SST anomaly of the i-th grid in the p-th patch. $\frac{\partial R}{\partial SST_P}$ is the sensitivity of R to patch-averaged SST change, which is derived from experiments for the corresponding patch warming and cooling experiments. The sensitivity for grid boxes within a single patch corresponds to the average R change due to a 1 K warming within that specific grid box. The sensitivities of polar energy budget to SST perturbation in each grid box are shown in Figure 4.

Utilizing these sensitivities, we can reconstruct the polar energy budget response to arbitrary changes in SST through the Green's function approach, represented as:

8

$$\Delta R = \Sigma_i \frac{\partial R}{\partial SST_i} \Delta SST_i + \varepsilon_I \, , \qquad\qquad\qquad\qquad\qquad\qquad\qquad\qquad (8)$$

where ε_I is an error term, which represents the contributions from nonlinearities and non-SST induced factors.

Then we use the Green's function approach to reconstruct the ΔR_{AHT} in response to 8 different SST patterns in the EOF-SST

205   experiments (Figures. 5a-h), and the Green's function reconstructed ΔR_{AHT} are then compared to model-produced values in

the EOF-SST experiments (Figures. 5i-j). The results show that the majority of the experimental simulations of ΔR_{AHT} align

closely with the ΔR_{AHT} reconstructed by the Green's function, lying near the y = x line. The biases of the Green's function

reconstructed values are partially induced by the SST change inside the Arctic region, which is not captured by the Green's

function reconstruction, and non-linear terms also contribute to the bias. Therefore, the Green's function approach can

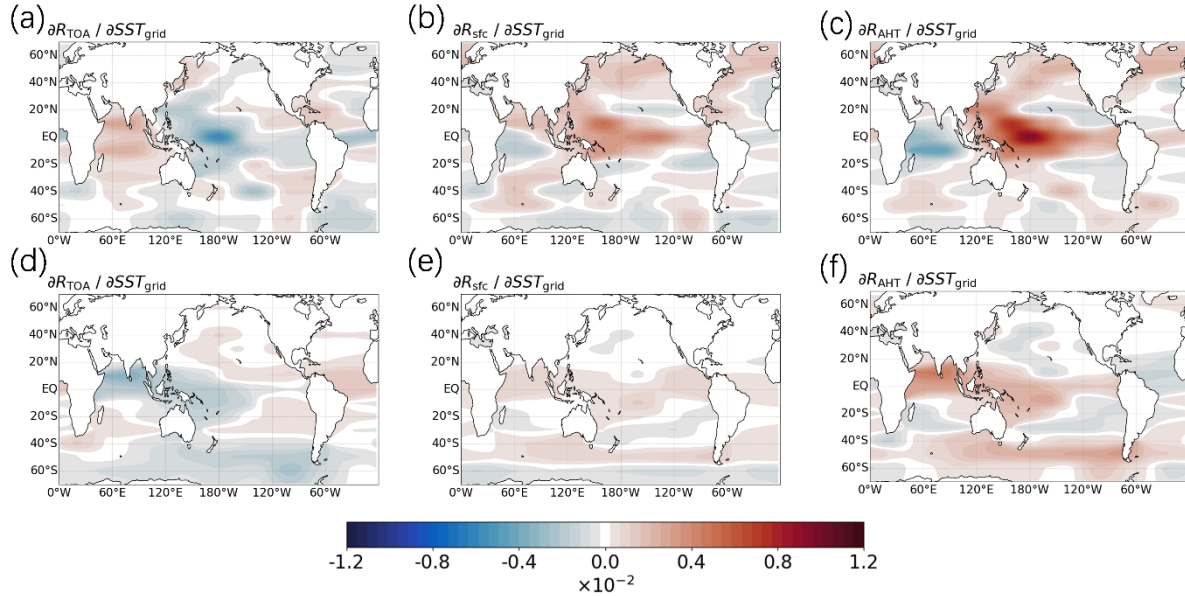210   qualitatively explain how the SST perturbation patterns in Figure 5(a-h) affects polar energy budget.

Figure 4: The sensitivity of (a) $\partial R_{TOA}/\partial SST_i$ of Arctic, (b) $\partial R_{sfc}/\partial SST_i$ of Arctic, (c) $\partial R_{AHT}/\partial SST_i$ of Arctic, (d) $\partial R_{TOA}/\partial SST_i$ of Arctic, (e) $\partial R_{sfc}/\partial SST_i$ of Arctic, (f) $\partial R_{AHT}/\partial SST_i$ of Antarctica to surface warming in each grid box, calculated using Eq. (7). The units are W/m²/K.
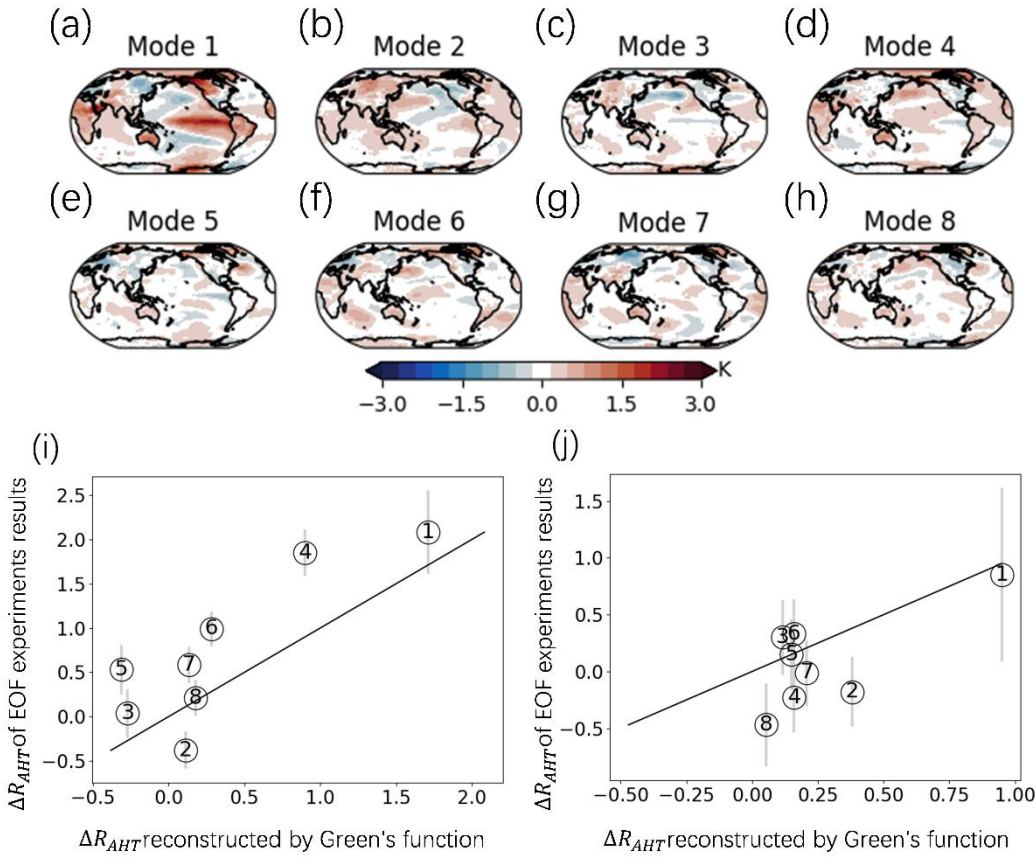
Figure 5: (a-h) The surface temperature change patterns in individual EOF-SST experiments. (i) Comparison of Arctic ΔR_{AHT} responses to different SST change patterns in EOF-SST experiments (y-axis) and that reconstructed by the Green's function approach (x-axis). All values are averaged annually in this figure. The digits represent the number of corresponding EOF modes in each experiment. Error bars correspond to the 95 % confidence interval. (j) Response of Antarctica ΔR_{AHT}.

3.3 Decomposition of polar energy budget responses with radiative kernels

To understand the mechanism how polar energy budget is affected by remote SST, we quantify the contributions of meteorological factors to polar energy budget responses (Figures 6-7) using radiative kernels (Huang et al., 2017). Figure 6a shows that the contribution of cloud changes is relatively small to the Arctic ΔR_{TOA} response. Pacific SST warming results in a negative Arctic $\Delta R_{TOA,cld}$, whereas Indian Ocean warming generates a positive Arctic $\Delta R_{TOA,cld}$. Albedo exhibits a positive response in both the tropical Indian Ocean and the Pacific Ocean (Figure 6a). The impact of Arctic $\Delta R_{TOA,plk}$ exhibits a positive response to SST increases in the tropical Indian Ocean and a negative response to the

10

tropical western Pacific (Figure 6c), indicating that the Planck feedback is the primary contributor to Arctic ΔR_{TOA}. The sensitivity of Arctic $\Delta R_{TOA,LR}$ to SST increases exhibits a negative response to warming in the tropical western Pacific, while showing a positive response in the Indian Ocean (Figure 6d). The Planck feedback's response to SST warming is approximately twice that of the lapse-rate feedback.

For the Antarctic, the contribution of clouds to the ΔR_{TOA} response is minimal (Figure 6f), as is the contribution of albedo changes to the Antarctic ΔR_{TOA} response (Figure 6e). In contrast to the Arctic, the Antarctic ΔR_{TOA} response to SST changes is jointly dominated by Planck and lapse-rate feedbacks. Warming in the Indian Ocean induces a stronger negative $\Delta R_{TOA,plk}$ (Figure 6g), whereas warming in the Pacific leads to a more pronounced negative $\Delta R_{TOA,LR}$ (Figure 6h). Additionally, warming in the tropical Atlantic triggers a notably strong positive $\Delta R_{TOA,LR}$ (Figure 6h).
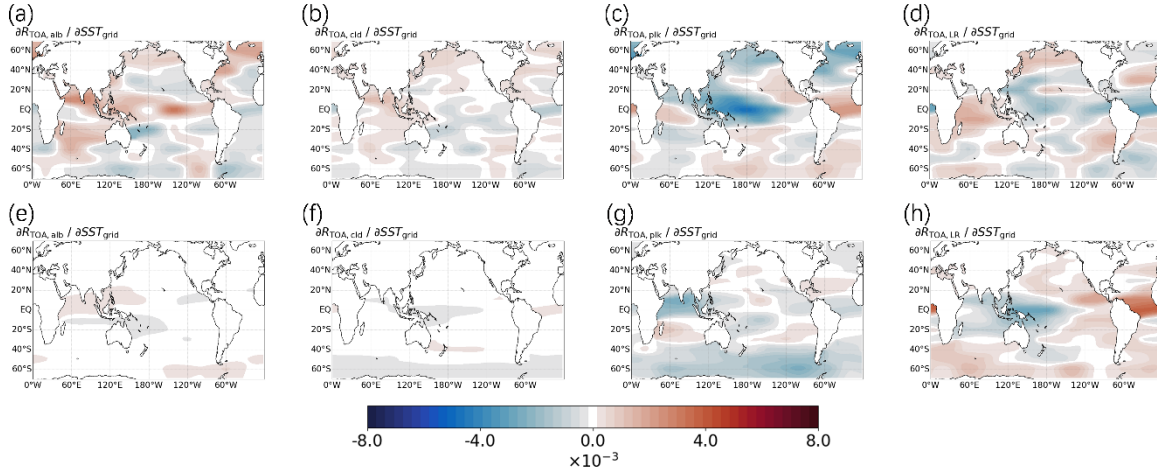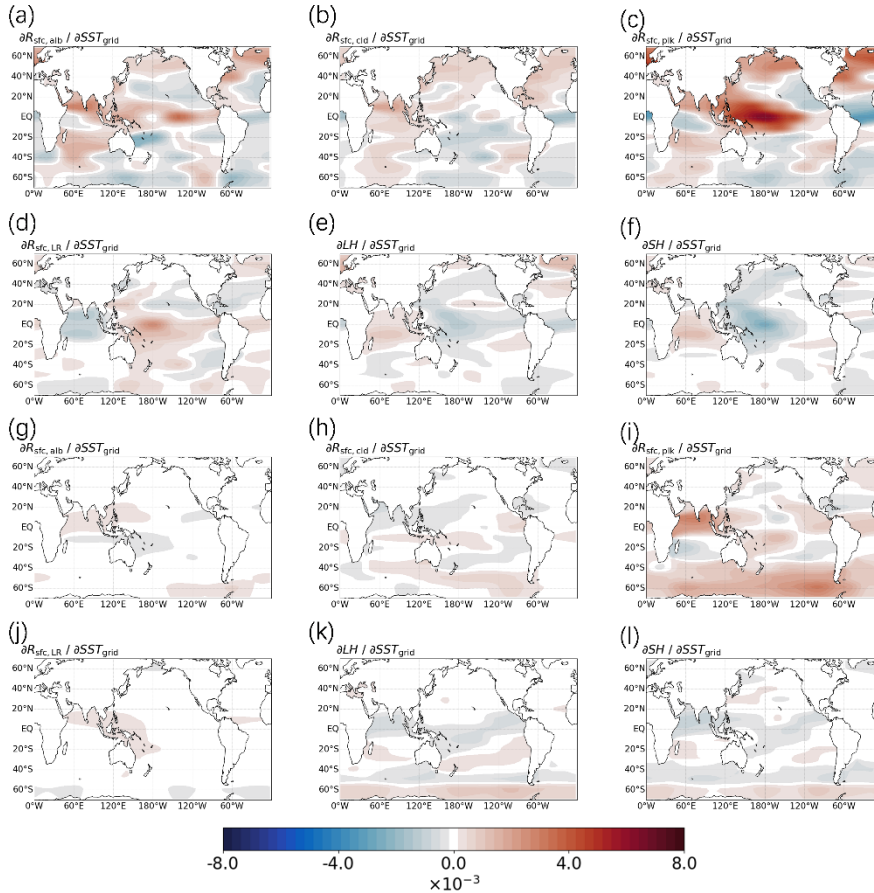

Figure 6: Difference of annual mean $\Delta R_{TOA,cld}$ (a), $\Delta R_{TOA,alb}$ (b) , $\Delta R_{TOA,plk}$ (c) , $\Delta R_{TOA,LR}$ (d) for Arctic and annual mean $\Delta R_{TOA,cld}$(e), $\Delta R_{TOA,alb}$(f) , $\Delta R_{TOA,plk}$(g) , $\Delta R_{TOA,LR}$(h) for Antarctica between conjugate warming and cooling patch experiments.

Figure 7 shows the contributions of meteorological factors to the responses of Arctic and Antarctic ΔR_{sfc}. For the Arctic, the spatial distribution of clouds' contribution to Arctic ΔR_{sfc} is similar to that for Arctic ΔR_{TOA}, but the values are significantly higher (Figure 7b). The response of Arctic $\Delta R_{sfc,alb}$ closely resembles that of $\Delta R_{TOA,alb}$, with similar magnitudes (Figure 7a). Similar to the response of Arctic $\Delta R_{TOA,plk}$, the Arctic $\Delta R_{sfc,plk}$ response is also strong (Figure 7c), but the signs of $\Delta R_{sfc,plk}$ responses are generally opposite to those of $\Delta R_{TOA,plk}$ response. The response of Arctic $\Delta R_{sfc,LR}$ to tropical ocean warming also shows signs opposite to those of $\Delta R_{TOA,LR}$ (Figure 7d). Over the tropical Indian Ocean, Planck feedback is positive in the northern region and negative in the southern region, whereas lapse-rate feedback is consistently negative across the entire tropical Indian Ocean. Overall, Planck feedback remains dominant for the Arctic ΔR_{sfc}. The responses of Arctic ΔLH and Arctic ΔSH are negative in response to warmings in the tropical western Pacific and positive in response to warmings in the tropical Indian Ocean (Figure 7e, f), though these factors have a minor impact on Arctic ΔR_{sfc}. The negative responses of

11

Arctic ΔLH and ΔSH in response to warmings in the tropical western Pacific indicate a suppression of upward turbulent heat fluxes at the Arctic surface, primarily due to enhanced energy transport from lower latitudes into the Arctic region. As warm air masses are advected poleward, the associated increase in downward longwave radiation warms the Arctic surface. This

255 warming stabilizes the lower atmospheric boundary layer, thereby reducing the vertical turbulence necessary for effective heat exchange between the surface and the atmosphere.

Similar to the Arctic regions, the contribution of cloud to Antarctic ΔR_{sfc} is small (Figure 7h). Albedo has no significant impact on Antarctic ΔR_{sfc} (Figure 7g), because sea ice concentration is fixed in these patch experiments and snow cover in Antarctica does not change significantly in these experiments. The Planck feedback dominates the contributions to Antarctic

260 ΔR_{sfc}, with Antarctic $\Delta R_{sfc,plk}$ responding positively to tropical ocean warming (Figure 7i). Similar to the Arctic, the lapse-rate feedback contributes less significantly to ΔR_{sfc} (Figure 7j). Antarctic ΔLH and ΔSH show minimal responses with opposite signs to $\Delta R_{sfc,plk}$ (Figures 7k, l). These results suggest that while temperature adjustments are notable in Antarctica, responses of cloud cover and surface heat fluxes to remote SST warming have a small impact on Antarctic ΔR_{sfc}.

Figure 7: Difference of annual mean $\Delta R_{sfc,cld}$**(a),** $\Delta R_{sfc,alb}$**(b) ,** $\Delta R_{sfc,plk}$**(c) ,** $\Delta R_{sfc,LR}$**(g),** ΔLH **(h),** ΔSH **(i) for the Arctic region, and annual mean** $\Delta R_{sfc,cld}$**(d),** $\Delta R_{sfc,alb}$**(e) ,** $\Delta R_{sfc,plk}$**(f) ,** $\Delta R_{sfc,LR}$**(j) ,** ΔLH **(k),** ΔSH **(l) for the Antarctic region between conjugate warming and cooling patch experiments.**

3.4 AHT responses to Regional SST Changes

According to Figures (6-7), the Planck feedback, which is primarily driven by changes in temperature, is the primary contributor to polar energy budget responses in these experiments. The sign of ΔR_{AHT} is generally same as $\Delta R_{sfc,plk}$, and opposite from $\Delta R_{TOA,plk}$. In addition, the difference between TOA and surface energy budget reflects the contribution of changes in polar AHT. Therefore, AHT plays a critical role in determining polar energy budget by changing the air temperature of polar regions. The responses of AHT to SST perturbations in the midlatitudes are consistent with our intuition, but the opposite Arctic AHT responses to SST warming over the tropical Indian Ocean and tropical Pacific Ocean requires further investigations.

To explore the underlying mechanisms of this phenomenon, we compare the climate responses to warmings in two illustrative patches within the tropical Pacific Ocean (TPO) and Indian Ocean (TIO). The center of the illustrative TPO patch is (180°E, 0°N), and the center of the illustrative TIO is (60°E, 0°N).

Figure 8 presents the responses of surface temperature (ΔT_s), 200hPa geopotential height (ΔZ_{200}), and 500hPa geopotential height (ΔZ_{500}) to warmings in these patches, providing background information to later AHT studies. Consistent with previous studies (Annamalai et al., 2007; Barsugli & Sardeshmukh, 2002; Ding et al., 2014), our experiments reveal that SST anomalies in different ocean basins induce contrasting atmospheric circulation patterns, primarily through Rossby wave responses affecting the Pacific-North American (PNA) pattern.

Specifically, warming in the TPO region leads to ΔT_s increase over the Tibetan Plateau, Eastern Europe, tropical Africa, northeastern North America, and most of Antarctica. Concurrently, ΔZ_{200} exhibits a local increase over the TPO region, a decrease over the North Pacific, and increases over north-eastern North America and Antarctica. The ΔZ_{500} response mirrors the ΔZ_{200} pattern but with reduced intensity. In contrast, warming in the TIO region induces ΔT_s increases over Antarctica and significant warming over the Indian subcontinent, while the Tibetan Plateau experiences cooling. Notably, the northwest of North America shows marked cooling under TIO warming. The ΔZ_{200} response to TIO warming displays a dipole pattern, characterized by increases in the tropical warming regions and decreases toward the poles, followed by subsequent increases. The ΔZ_{500} response follows a similar trend to ΔZ_{200} with weaker intensity.
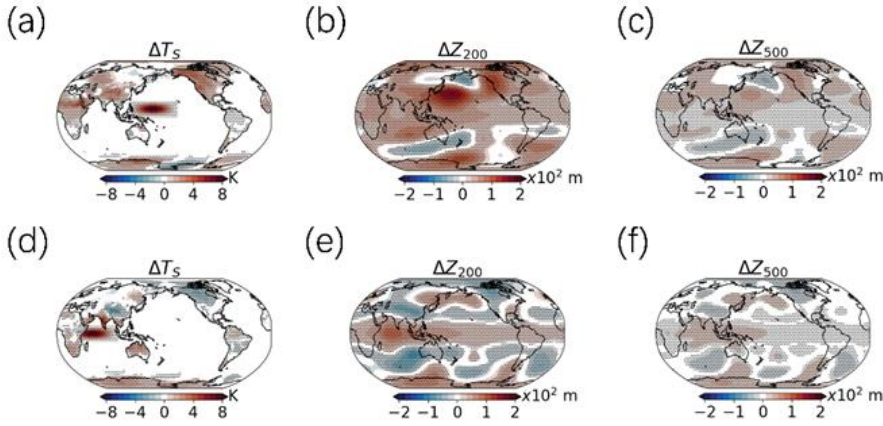
Figure 8: Spatial distributions of responses in ΔT_s (a), ΔZ_{200} (b) and ΔZ_{500} (c) following increased SST in a patch over the tropical Pacific Ocean (TPO), and in ΔT_s (d), ΔZ_{200} (e) and ΔZ_{500} (f) following increased SST in a patch over the tropical Indian Ocean (TIO). Dotted areas indicate regions that passed the 95% confidence test.

To quantify the impacts of SST warming over the TPO and TIO on the Arctic AHT, we computed the AHT responses to the warming of the two patches separately. AHT can be calculated as the vertically integrated and zonally averaged transport of moist static energy (S). According to Neelin and Held (1987), S can be defined as follows:

$$S = c_p T_a + LQ + gZ, \tag{9}$$

where T_a represents atmospheric temperature, c_p is the specific heat capacity of air at constant pressure, L denotes the latent heat of vaporization of water, Q is specific humidity, g is the acceleration due to gravity, and Z represents geopotential height. The components of S will be denoted below as S_T, S_Q, and S_Z, respectively.

The poleward transport of moist static energy S can be decomposed into mean meridional circulation (MOC), stationary eddy (SE), transient eddy (TE), and transient overturning circulation (TOC) components, following the methodologies of Priestley (1948) and Lorenz (1953). According to Donohoe (2020), for each latitude θ, atmospheric energy transport is:

$$AHT(\theta) = 2\pi\, a cos(\theta) \int_0^{P_s} [\bar{V}][\bar{S}] + \overline{[V^*S^*]} + \overline{[V'^*S'^*]} + \overline{[V]'[S]'} \frac{dp}{g}, \tag{10}$$

where V represents the meridional velocity. Square brackets [ ] denote zonal averages, overbars $\overline{(\ )}$ denote time averages over each month of analysis, asterisks (*) are departures from the zonal average, and primes (') are departures from the time average. The first term signifies the MOC driven by the vertical gradient in S, taking into account mass conservation in MOC energy transport. The second term is SE, showing poleward transport in warm or moist sectors. These first two terms can be calculated from monthly mean data. The third term pertains to the transport associated with TE, primarily baroclinic synoptic eddies. The fourth term involves energy transport by the covariance between zonal-mean overturning circulation

14

315 and vertical stratification, referred to as TOC, which is significantly smaller than the other components and thus often

excluded in AHT discussions.

Figure 9 shows the changes in AHT and its components in response to warmings in the TPO and TIO. AHT response to

warmings in TPO at 60°N is positive, and AHT response to warmings in TIO at 60°N is negative. For both cases, AHT to

the Arctic region is dominated by SE (Figure 9b), and the opposite SE response to TPO and TIO leads to opposite responses

320 in AHT, which also causes different responses of TOA and surface energy budgets in the Arctic regions. Additionally,

Figures 9c and 9d further dissect the SE responses to warmings in the TPO and TIO, respectively, and the results indicate

that dry static energy predominantly drives the SE response to warmings in both TPO and TIO.
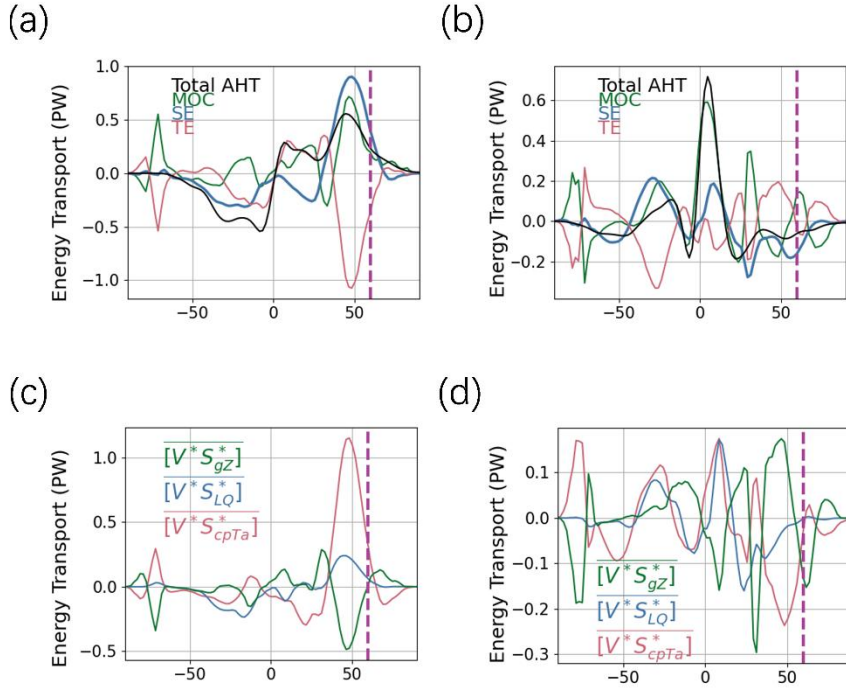
325 **Figure 9: Decomposition of meridional AHT. (a) and (b) show the changes in meridional AHT following SST**
warming in the TPO and TIO, respectively. The total AHT is represented by a thick black line, while the
contributions from the MOC, SE, and TE are depicted by fine lines in green, blue, and red, respectively. Panels (c)
and (d) detail the decomposition of the SE component from (a) and (b), with the contributions from Z, Q, and T
shown in green, blue, and red, respectively. The purple dotted line represents the 60°N latitude line.

330

To better understand the opposite response of SE heat flux to warmings in TPO and TIO, we analyzed the spatial distribution

of SE heat fluxes. The vertically integrated SE heat flux (ϕ) can be computed through the following integral :

$$\phi = \int_0^{P_s} V^* S^* \frac{dp}{g}, \tag{11}$$

In response to warmings in the TPO, the vertically integrated SE heat flux exhibits significant oscillatory characteristics over
335   the Pacific Ocean. According to Figure 10(a), ϕ increases in the western tropical and north-west Pacific, decreases over the
central Pacific, and then increases again over the northeastern Pacific and Alaska. Over land, ϕ increases over north-east
Asia, the Tibetan Plateau and Europe. This phenomenon is consistent to Goss et al. (2016), who found that warming in the
low-latitude Pacific leads to increased ϕ in higher latitudes.

Combining Eqs. (9) and (11), we are able to further attribute ϕ to changes in dry static heat flux ($\Delta\phi_{Ta}$), latent heat flux
340   ($\Delta\phi_Q$), and potential energy ($\Delta\phi_Z$), respectively. Among the three main contributing factors to $\Delta\phi$, $\Delta\phi_{Ta}$ aligns closely with
the overall $\Delta\phi$ pattern, indicating it as the primary contributor (Figure 10b). The spatial pattern of $\Delta\phi_{Ta}$ can be explained by
the change of ΔV^* and $\Delta S_{Ta}{}^*$ (Figs 10c-d), which reflects the spatial pattern of stationary waves. In addition, $\Delta\phi_Q$ is large in
the low latitudes, but is small near the poles (Figure 10e). Interestingly, the $\Delta\phi_Z$ exhibits an opposite pattern to $\Delta\phi$ in the
northern hemisphere (Figure 10f). Despite the changes in $\Delta S_Z{}^*$ have a similar spatial distribution to $\Delta S_{Ta}{}^*$ (Figure 10h), $\Delta\phi_Z$
345   shows an opposite trend to $\Delta\phi_{Ta}$ due to the differing correlation between ΔV^* and $\Delta S_Z{}^*$. This indicates that while $\Delta S_Z{}^*$
increases in regions where ΔV^* also increases, their combined effect on $\Delta\phi_Z$ leads to a negative contribution compared to
$\Delta\phi$.

In response to warmings in the TIO, the spatial pattern of $\Delta\phi$ oscillation is quite different from the TPO case. The transfer of
SE heat flux encounters obstacles near the Tibetan Plateau, which might explain why the response of $\Delta\phi$ is different in the
350   Northern hemisphere and the Southern hemisphere. Globally, $\Delta\phi_{Ta}$ remains the dominant contributor to $\Delta\phi$, while $\Delta\phi_Q$'s
contribution remains relatively low. Notably, in the Tibetan Plateau region, $\Delta\phi_Z$ becomes the primary driver of $\Delta\phi$ (Figures
10i, n).

Based on these results, we are able to understand why the responses of AHT near 60°N to warmings in TPO and TIO are
different. The response of stationary waves to warmings in these two regions are different, so the poleward moist static
355   energy transported by SE is also different, leading to opposite AHT responses. These findings support the research results of
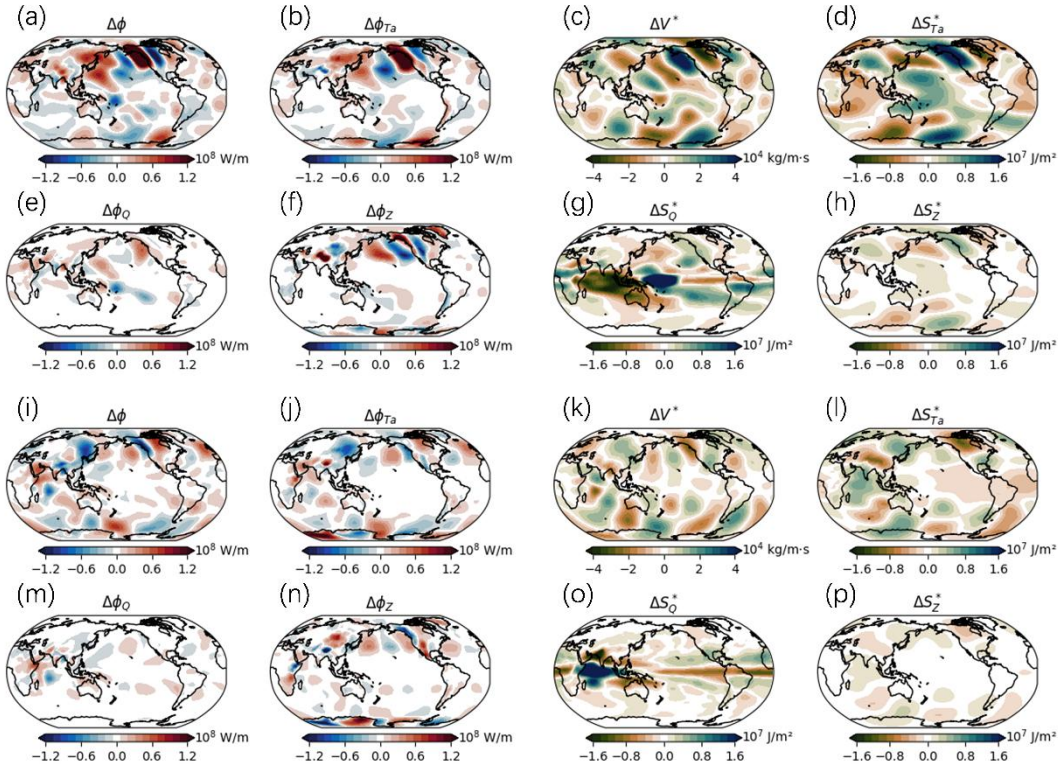Goss et al. (2016) and the tropical excitation mechanism for Arctic warming outlined by Lee et al. (2011).

16

Figure 10: (a) $\Delta\phi$ induced by SST warming in the TPO. (b) The contribution of $\Delta\phi_{Ta}$ to the SE. (c) The vertical integration of ΔV^* from the surface to the TOA. (d) The vertical integration of ΔS_{Ta}^* from the surface to the TOA. (e) The contribution of $\Delta\phi_Q$ to the SE. (f) The contribution of $\Delta\phi_Z$ to the SE. (g) The vertical integration of ΔS_Q^* from the surface to the TOA. (h) The vertical integration of ΔS_Z^* from the surface to the TOA. (i-p) are same as (a-h) but for responses to warming in the TIO.

4 Conclusion

This study delves into the mechanisms behind the responses of radiative budget in high-latitude regions to sea surface warmings in the low latitudes through a series of idealized SST change experiments. It elucidates the mechanisms through which the polar energy budget responds to distant SST variations, revealing significant different impacts of SST changes across different oceanic regions on the Arctic and Antarctic energy budgets. These impacts are mediated by alterations in AHT, the distribution of sensible heat flux from stationary eddies, and the interactions among various climatic drivers such as temperature, humidity, and cloud radiative processes.

Specifically, increases in SST in the Pacific and Indian Oceans have opposite effects on the Arctic polar energy budget in Boreal winter, attributable to different responses of stationary waves to warming in these oceans, which subsequently alter

17

the patterns of poleward AHT. Warming in the Pacific SST tends to enhance heat transport to the Arctic, leading to Arctic air temperature increases, whereas warming in the Indian Ocean reduces the heat transport towards the Arctic, resulting in

375 Arctic air temperature decreases. Additionally, the study highlights that the response of the polar energy budget varies with the season. During Boreal winter, the sensitivity of the Arctic polar energy budget to SST changes in tropical regions is stronger, indicating a higher sensitivity of the polar region to tropical ocean warming in winter. Using radiative kernels, the contributions of meteorological factors to the TOA radiation response were quantified. The results indicate that changes in Planck feedback is the primary contributor to changes in polar TOA radiation, while the contributions from clouds and

380 albedo are relatively small. The decomposition of surface radiation also shows that the Planck feedback plays a primary role in driving changes in polar surface radiation. Finally, the study reconstructed the AHT responses under different EOF-SST modes using the Green's function approach, validating the consistency between the model experiment results and the Green's function reconstructions. Although biases exist in certain EOF modes, partially due to SST changes within the polar regions and non-linear effects, the Green's function method generally provides a reasonable reconstruction of the polar energy

385 budget response to SST changes.

The primary findings of the study are summarized as follows:

1. In response to SST warmings in most tropical and midlatitude regions, polar air temperatures increase due to enhanced AHT, leading to an increase in the polar surface energy budget and a decrease in the polar TOA energy budget.

2. The response of Arctic AHT to warmings in the tropical Indian Ocean is negative in Boreal winter. Stationary eddies

390 play a crucial role in modulating the polar AHT response to tropical SST changes.

3. Subtropical SST changes have relatively weak impacts on the polar energy budget.

The findings of this study have implications for understanding and predicting polar climate responses to global warming. The distinct responses of the Arctic and Antarctic energy budgets to regional SST changes underscore the necessity of considering regional specificity when modeling and predicting climate change. The different impacts of SST changes in

395 various oceanic regions on the polar energy budgets highlight the importance of incorporating regional specificity in climate models. Moreover, the study underscores the important role of AHT in modulating polar temperatures, and emphasize the critical role of radiative feedbacks in shaping the polar climate. Understanding the mechanisms of AHT and its interaction with stationary eddies can lead to improved predictions of polar climate responses to global SST changes. The analyses of radiative feedbacks, including the roles of temperature, humidity, and clouds, provide a comprehensive understanding of the

400 factors contributing to polar amplification. Results from only one global climate model are analyzed in this study, and analyses with more climate models from the Green's function model intercomparison project (GFMIP, Bloch-Johnson et al., 2024) might be useful to reduce model biases in future studies.

Author Contributions

405   Methodology: C.Z.;

Investigation: Q.W.;

Writing – original draft preparation: Q.W.;

Writing – review & editing: C.Z., Y.L., L.Z.

Code Availability

410   The code used in this study are available upon request from the corresponding author.

Competing interests

415   The contact author has declared that none of the authors has any competing interests.

References

Alexeev, V. A., Langen, P. L., and Bates, J. R.: Polar amplification of surface warming on an aquaplanet in "ghost forcing" experiments without sea ice feedbacks, Clim. Dyn., 24, 655–666, https://doi.org/10.1007/s00382-005-0018-3, 2005.

420   Annamalai, H., Okajima, H., and Watanabe, M.: Possible impact of the Indian Ocean SST on the Northern Hemisphere circulation during El Niño, J. Climate, 20, 3164–3189, https://doi.org/10.1175/JCLI4156.1, 2007.

Baggett, C. and Lee, S.: An identification of the mechanisms that lead to Arctic warming during planetary-scale and synoptic-scale wave life cycles, J. Atmos. Sci., 74, 1859–1877, https://doi.org/10.1175/JAS-D-16-0156.1, 2017.

Barsugli, J. J. and Sardeshmukh, P. D.: Global atmospheric sensitivity to tropical SST anomalies throughout the Indo-Pacific

425   basin, J. Clim., 15, 3427–3442, https://doi.org/10.1175/1520-0442(2002)015<3427>2.0.CO;2, 2002.

Barton, N. P., Klein, S. A., Boyle, J. S., and Zhang, Y. Y.:Arctic synoptic regimes: Comparing domain-wide Arctic cloud observations with CAM4 and CAM5 during similar dynamics., 117, D15205, https://doi.org/10.1029/2012JD017589, 2012.

Bloch-Johnson, J., Rugenstein, M. A. A., Alessi, M. J., Proistosescu, C., Zhao, M., Zhang, B., Williams, A. I. L., Gregory, J. M., Cole, J., Dong, Y., Duffy, M. L., Kang, S. M., and Zhou, C..：The Green's Function Model Intercomparison Project

430　(GFMIP) Protocol, J. Adv. Model. Earth Syst., 16, e2023MS003700, https://doi.org/10.1029/2023MS003700, 2024.

Boeke, R. C. and Taylor, P. C.: Seasonal energy exchange in sea ice retreat regions contributes to differences in projected Arctic warming, Nat. Commun., 9, 5017, https://doi.org/10.1038/s41467-018-07061-9, 2018.

Budyko, M. I.: The effect of solar radiation variations on the climate of the Earth, Tellus, 21, 611–619, https://doi.org/10.3402/tellusa.v21i5.10109, 1969.

435　Cao, G. and Zhang, G. J.: Role of vertical structure of convective heating in MJO simulation in NCAR CAM5.3, J. Clim., 30, 7423–7439, https://doi.org/10.1175/JCLI-D-16-0913.1, 2017.

Chung, C. E. and Räisänen, P.: Origin of the Arctic warming in climate models, Geophys. Res. Lett., 38, L21704, https://doi.org/10.1029/2011GL049816, 2011.

Dai, A., Luo, D., Song, M., and Liu, J.: Arctic amplification is caused by sea-ice loss under increasing CO_2, Nat. Commun.,

440　10, 121, https://doi.org/10.1038/s41467-018-07954-9, 2019.

Dickinson, R. E., Meehl, G. A., and Washington, W. M.: Ice-albedo feedback in a CO2-doubling simulation, Climatic Change, 10, 241–248, https://doi.org/10.1007/BF00143904, 1987.

Ding, Q., Wallace, J. M., Battisti, D. S., and Steig, E. J.: Tropical forcing of the recent rapid Arctic warming in northeastern Canada and Greenland, Nature, 509, 209–212, https://doi.org/10.1038/nature13260, 2014.

445　Donohoe, A., Armour, K. C., Roe, G. H., Battisti, D. S., and Hahn, L.: The partitioning of meridional heat transport from the last glacial maximum to CO2 quadrupling in coupled climate models, J. Clim., 33, 4141–4165, https://doi.org/10.1175/JCLI-D-19-0797.1, 2020.

Duan, L., Cao, L., and Caldeira, K.: Estimating contributions of sea ice and land snow to climate feedback, J. Geophys. Res. Atmos., 124, 199–208, https://doi.org/10.1029/2018JD029093, 2019.

450　Fletcher, C. G. and Kushner, P. J.: The role of linear interference in the annular mode response to tropical SST forcing, J. Clim., 24, 778–794, https://doi.org/10.1175/2010JCLI3735.1, 2011.

Goosse, H., Kay, J. E., Armour, K. C., Bodas-Salcedo, A., Chepfer, H., Docquier, D., Jonko, A., Kushner, P. J., Lecomte, O., Massonnet, F., Park, H.-S., Pithan, F., Svensson, G., and Vancoppenolle, M.: Quantifying climate feedbacks in polar regions, Nat. Commun., 9, 1919, https://doi.org/10.1038/s41467-018-04173-0, 2018.

455　Goss, M., Feldstein, S. B., and Lee, S.: Stationary wave interference and its relation to tropical convection and Arctic warming, J. Clim., 29, 1369–1389, https://doi.org/10.1175/JCLI-D-15-0267.1, 2016.

Graversen, R. G. and Burtu, M.: Arctic amplification enhanced by latent energy transport of atmospheric planetary waves, Q.J.R. Meteorol. Soc., 142, 2046–2054, https://doi.org/10.1002/qj.2802, 2016.

Hahn, L. C., Armour, K. C., Zelinka, M. D., Bitz, C. M., and Donohoe, A.: Contributions to polar amplification in CMIP5 and

460　CMIP6 models, Front. Earth Sci., 9, 710036, https://doi.org/10.3389/feart.2021.710036, 2021.

Hall, A.: The Role of Surface Albedo Feedback in Climate, J. Clim., 17, 1550–1568, https://doi.org/10.1175/1520-0442(2004)017<1550>2.0.CO;2, 2004.

Huang, Y., Ma, M.-L., and Tung, K.-K.: Radiative feedbacks and the polar amplification of surface temperature change, J. Geophys. Res.-Atmos., 122, 4565-4577, https://doi.org/10.1002/2017JD027221, 2017.

465 Jeong, H., Park, H.-S., Stuecker, M. F., and Yeh, S.-W.: Distinct impacts of major El Niño events on Arctic temperatures due to differences in eastern tropical Pacific sea surface temperatures, Sci. Adv., 8, eabl8278, https://doi.org/10.1126/sciadv.abl8278, 2022.

Laîné, A., Yoshimori, M., and Abe-Ouchi, A.: Surface Arctic amplification factors in CMIP5 models: Land and oceanic surfaces and seasonality, J. Clim., 29, 3297–3316, https://doi.org/10.1175/JCLI-D-15-0497.1, 2016.

470 Lee, S., Gong, T. T., Johnson, N. C., Feldstein, S. B., and Pollard, D.: On the possible link between tropical convection and the Northern Hemisphere Arctic surface air temperature change between 1958 and 2001, J. Clim., 24, 4350–4367, https://doi.org/10.1175/2011JCLI4003.1, 2011.

Lee, S.: Testing of the Tropically Excited Arctic Warming Mechanism (TEAM) with Traditional El Niño and La Niña, J. Clim., 25, 4015–4022, https://doi.org/10.1175/JCLI-D-12-00055.1, 2012.

475 Lee, S.: A Theory for Polar Amplification from a General Circulation Perspective, Asia-pacific J. Atmos. Sci., 50, 31–43, https://doi.org/10.1007/s13143-014-0024-7, 2014.

Lenssen, N. J. L., Schmidt, G. A., Hansen, J. E., Menne, M. J., Persin, A., Ruedy, R., et al.: Improvements in the GISTEMP uncertainty model, J. Geophys. Res. Atmos., 124, 6307–6326, https://doi.org/10.1029/2018JD029522, 2019.

Li, Z.-X. and Le Treut, H.: Cloud-radiation feedbacks in a general circulation model and their dependence on cloud modelling

480 assumptions, Clim. Dyn., 7, 133–139, https://doi.org/10.1007/BF00211155, 1992.

Li, X., Cai, W., Meehl, G.A. et al. Tropical teleconnection impacts on Antarctic climate changes. Nat Rev Earth Environ., 2, 680–698, https://doi.org/10.1038/s43017-021-00204-5, 2021.

Liu, Y., Huang, Y., Yuan, J., Xie, Y., Zhou, C.: Contribution of surface radiative effects, heat fluxes and their interactions to land surface temperature variability, *J. Geophys. Res. Atmos.*, 129, e2023JD039495, https://doi.org/10.1029/2023JD039495,

485 2024.

Lorenz, E. N.: Available potential energy and the maintenance of the general circulation, Tellus, 7, 157–167, 1955.

Marshall, G. J.: Trends in the Southern Annular Mode from observations and reanalyses, J. Climate, 16, 4134–4143, https://doi.org/10.1175/1520-0442(2003)016<4134>2.0.CO;2, 2003.

Mitchell, J. F. B., Senior, C. A., and Ingram, W. J.: CO2 and climate: a missing feedback?, Nature, 341, 132–134,

490 https://doi.org/10.1038/341132a0, 1989.

Neale, R. B., and Coauthors: Description of the NCAR Community Atmosphere Model (CAM 5.0), https://doi.org/10.5065/D6N877R0, 2012.

Neelin, J. D. and Held, I. M.: Modeling tropical convergence based on the moist static energy budget, Mon. Weather Rev., 115, 3–12, https://doi.org/10.1175/1520-0493(1987)115<0003>2.0.CO;2, 1987.

495   Park, H.-S., Kim, S.-J., Seo, K.-H., Stewart, A. L., Kim, S.-Y., and Son, S.-W.: The impact of Arctic sea ice loss on mid-Holocene climate, Nat. Commun., 9, 4571, https://doi.org/10.1038/s41467-018-07068-2, 2018.

Pierrehumbert, R. T.: Principles of Planetary Climate, Cambridge University Press, Cambridge, UK, 2010.

Pithan, F., Medeiros, B., and Mauritsen, T.: Mixed-phase clouds cause climate model biases in Arctic wintertime temperature inversions, Clim. Dyn., 43, 289–303, https://doi.org/10.1007/s00382-013-1964-9, 2014.

500   Priestley, C. H. B.: Dynamical control of atmospheric pressure: II—the size of pressure systems, Q. J. R. Meteorol. Soc., 74, 67–72, https://doi.org/10.1002/qj.49707431908, 1948.

Rodgers, K. B.: A tropical mechanism for Northern Hemphere deglaciation, Geochem.Geophys.Geosyst., 4, 1046, https://doi.org/10.1029/2003gc000508, 2003.

Salzmann, M.: The polar amplification asymmetry: Role of Antarctic surface height, Earth Syst. Dynam., 8, 323–336,
505   https://doi.org/10.5194/esd-8-323-2017, 2017.

Sellers, W. D.: A Global Climatic Model Based on the Energy Balance of the Earth-Atmosphere System, J. Appl. Meteorol., 8, 392–400, https://doi.org/10.1175/1520-0450(1969)008<0392>2.0.CO;2, 1969.

Sejas, S. A., and Cai, M.: Isolating the Temperature Feedback Loop and its Effects on Surface Temperature, J. Atmos. Sci., 73, 3287–3303, https://doi.org/10.1175/JAS-D-15-0287.1, 2016.

510   Semmler, T., Pithan, F., and Jung, T.: Quantifying two-way influences between the Arctic and mid-latitudes through regionally increased CO2 concentrations in coupled climate simulations, Clim. Dyn., 54, 3307–3321, https://doi.org/10.1007/s00382-020-05171-z, 2020.

Shaw, T. A. and Tan, Z.: Testing latitudinally dependent explanations of the circulation response to increased CO2 using aquaplanet models, Geophys. Res. Lett., 45, 9861–9869, https://doi.org/10.1029/2018GL078974, 2018.

515   Smith, D. M., Screen, J. A., Deser, C., Cohen, J., Fyfe, J. C., García-Serrano, J., et al.: The Polar Amplification Model Intercomparison Project (PAMIP) contribution to CMIP6: Investigating the causes and consequences of polar amplification, Geosci. Model Dev., 12, 1139–1164, https://doi.org/10.5194/gmd-12-1139-2019, 2019.

Soden, B. J., Held, I. M., Colman, R., Shell, K. M., Kiehl, J. T., and Shields, C. A.: Quantifying climate feedbacks using radiative kernels, J. Climate, 21, 3504–3520, https://doi.org/10.1175/2007JCLI2110.1, 2008.

520   Solomon, A., Shupe, M. D., Persson, O., Morrison, H., Yamaguchi, T., Caldwell, P. M., et al.: The sensitivity of springtime Arctic mixed-phase stratocumulus clouds to surface-layer and cloud-top inversion-layer moisture sources, J. Atmos. Sci., 71, 574–595, https://doi.org/10.1175/JAS-D-13-0179.1, 2014.

Stuecker, M. F., Bitz, C. M., Armour, K. C., Proistosescu, C., Kang, S. M., Xie, S.-P., et al.: Polar amplification dominated by local forcing and feedbacks, Nat. Clim. Change, 8, 1076–1081, https://doi.org/10.1038/s41558-018-0339-y, 2018.

525   Taylor, P. C., Kato, S., Xu, K. M., and Cai, M.: Covariance between Arctic sea ice and clouds within atmospheric state regimes at the satellite footprint level, J. Geophys. Res. Atmos., 120, 12656–12678, https://doi.org/10.1002/2015JD023520, 2015.

Yoshimori, M., Abe-Ouchi, A., and Laîné, A.: The role of atmospheric heat transport and regional feedbacks in the Arctic warming at equilibrium, Clim. Dyn., 49, 3457–3472, https://doi.org/10.1007/s00382-017-3523-2, 2017.

Yu, Y., Taylor, P. C., and Cai, M.: Seasonal variations of Arctic low-level clouds and its linkage to sea ice seasonal variations, J. Geophys. Res. Atmos., 124, 12206–12226, https://doi.org/10.1029/2019JD031014, 2019.

Zhou, C., Zelinka, M. D., and Klein, S. A.: Analyzing the dependence of global cloud feedback on the spatial pattern of sea surface temperature change with a Green's function approach, J. Adv. Model. Earth Syst., 9, 2174–2189, https://doi.org/10.1002/2017MS001096, 2017.

Zhou, J., Lu, J., Hu, Y., and Zelinka, M. D.: Responses of the Hadley circulation to regional sea surface temperature changes, J. Clim., 33, 429–441, https://doi.org/10.1175/JCLI-D-19-0315.1, 2020.